



ARC Geophysical Research

Upscaling Transport and Sorption Processes via Spatial Markov Model in a Three-Dimensional Porous Domain

Giovanni Porta

o*1 and Elisa Baioni

o*2,3

 1 Department of Civil and Environmental Engineering, Politecnico di Milano, Italy 2 Univ Rennes, CNRS, Géosciences Rennes, France 3 Inria, Rennes, France

Abstract

The simulation of transport phenomena in porous media poses computational challenges related to the inherent heterogeneity and complexity of natural porous structures. In this work, we introduce a numerical tool grounded on the particle tracking method and the trajectory-based spatial Markov model (tSMM) to model pore-scale transport, as well as adsorption and desorption processes. The tSMM is an upscaling approach that accounts for the correlation between consecutive particle trajectory paths over a fixed distance, which enables predicting transport across larger scales. The SMM demonstrates accurate prediction of diffusive and adsorptive/desorptive phenomena, benchmarking the results against the direct numerical simulation outcomes. The method is based on an iterative procedure where each step is characterized by relying on a sample of simulated trajectories. The analysis demonstrates that selecting consecutive trajectories based on the outlet-inlet position provides more accuracy compared to assigning a uniform weight to each trajectory. The optimal parameterization of tSMM exhibits variability with Péclet numbers, underscoring a correlation between transport characteristics and the number of trajectories required for accurate predictions. Solute breakthrough at distinct locations reveals the impact of adsorptive Damköhler. Higher adsorptive Damköhler numbers lead to prolonged particle arrival times and distinctive arrival concentration patterns, that are closely matched by our low-cost upscaled approximation.

Keywords: Solute Transport, Adsorption, Porous Media, Upscaling, Random Walk Model

E-mail addresses: giovanni.porta@polimi.it

doi: 10.5149/ARC-GR.1654



^{*}Corresponding Author

1 Introduction

Accurate simulation of transport processes in porous media is crucial for understanding and managing subsurface flow and transport. Traditional numerical methods, face computational challenges when dealing with complex porous media structures at different scales. The heterogeneity of natural porous media across a broad range of scales often leads to complex and non-Fickian transport behavior, which challenges the conventional modeling approaches based on the advection-dispersion equation (ADE) [35]. Reactive phenomena can significantly increase the complexity of the problem. These processes can include chemical processes happening in the fluid phase or at the solid-liquid interface, as well as transformations activated by biological activity (e.g., presence of biofilm). In this context, obtaining accurate predictions at spatial scales significantly greater than those associated with individual pores is challenging [9]. This challenge is at the core of upscaling methods, whose aim is to embed pore-scale properties into effective parameters, thus enabling the accurate prediction through large-scale models.

In recent years, various upscaled models have been proposed to capture anomalous (non-Fickian) transport features across a wide range of temporal and spatial scales, such as the Continuous Time Random Walk (CTRW) [7, 8, 44, 45], Time-Domain Random Walk (TDRW) models [13, 28], fractional Advection-Dispersion models (fADE) [6, 18, 26, 43], and the Multirate Mass Transfer (MRMT) [16, 19, 29, 39]. In this work we focus particularly on the Spatial Markov Model (SMM) framework [22, 23]. The SMM relies on the computation of the travel time over a fixed distance and establishes a one-step correlation between consecutive travel times. The inclusion of this correlation enables leveraging information available on a limited portion of the system to predict transport over greater distances. This approach proves particularly effective in addressing advection-dominated scenarios, which pose difficulties for upscaling using traditional Eulerian approaches. SMMs have been successfully used to model conservative [11, 15, 17, 25, 30, 33] as well as reactive transport [37, 38, 40] in highly complex flows spanning from pore scales to much larger scales relevant in geology and subsurface hydrology. The SMM has been predominantly applied to one-dimensional transport settings, although some recent applications to multi-dimensional transport have been proposed in the literature [9, 12].

In this work, we introduce a numerical tool based on the particle tracking method to address transport problems and (linear) adsorption and desorption processes at pore-scale in a three-dimensional porous medium. The idea of using simulated trajectories to build a SMM approach has been proposed in previous works [27]. Specifically, we build our approach upon the trajectory-based spatial Markov model (tSMM) proposed by Sund et al. [38] and adapt it to operate in a three-dimensional domain. The methodology involves generating numerically simulated Lagrangian trajectories derived from a unit cell within the porous medium, which are then used to predict transport over significantly extended distances. This approach has mainly been employed to simulate transport and reactive surface processes on a periodic pore with idealized geometry [34, 36]. A preliminary version of this algorithm was introduced in [9], limited to upscaling transport in a two-dimensional pore-space. In addition, this work also upgrades the methodology proposed in [34] to simulate sorption/desorption phenomena coupled to transport. Numerical verification of the code is here rigorously conducted to assess convergence and performance scaling in the new context. Sorption/desorption reactions have a relevant influence on solute transport in environmental matrices as well as in lab-scale chromatographic characterization [1, 41]. The formal upscaling of sorption poses specific challenges as the surface reaction alters significantly the transport properties across multiple spatial and temporal scales [2, 5, 34, 42]. The algorithm has been implemented so that the extension to the third dimension does not cause performance issues, and the computational

effort is maintained within acceptable limits. Accurate optimization is ensured, including dynamic selection of the time step.

Our work involves benchmarking model results, expressed in terms of arrival times, number of adsorptions, and breakthrough concentration, against outcomes obtained from direct numerical simulations (DNS). A specific analysis is performed to evaluate the best approach for selecting the trajectory assigned to each particle, examining how the weight attributed to each trajectory impacts the numerical results. Additionally, we evaluate the influence of physical parameters, such as Péclet and Damköhler numbers, on transport and adsorption/desorption processes within the porous domain.

The paper is structured as follows: Section 2 provides a description of the methods, including pore-scale modeling and the upscaled SMM approach. The computational setup is detailed in Section 3, while Section 4 presents and discusses the numerical results. Concluding remarks from our study are summarized in Section 5.

2 Methodology

We consider solute transport and sorption/desorption processes in a periodic three-dimensional porous medium. The main characteristics of the implemented model are described in the following sections.

2.1 Pore-Scale Transport Setup

Let Ω be a three-dimensional porous domain fully saturated by a single fluid. The spatial domain is then divided into a solid Ω_s and fluid Ω_f phase, with Σ_{surface} defining the boundary surface between the two phases. We consider here the following pore-scale transport problem [34]

$$\frac{\partial C(\mathbf{x},t)}{\partial t} + \nabla \cdot [\mathbf{u}(\mathbf{x})C(\mathbf{x},t)] = \nabla \cdot [D\nabla C(\mathbf{x},t)] \quad \forall \quad \mathbf{x} \in \Omega_f$$

$$\frac{\partial S(\mathbf{x},t)}{\partial t} = -\lambda S(\mathbf{x},t) + \alpha C(\mathbf{x},t) = -D\frac{\partial C(\mathbf{x},t)}{\partial \mathbf{n}} \quad \forall \quad \mathbf{x} \in \Sigma_{\text{surface}}$$
(1)

where \mathbf{u} is the fluid velocity, C the concentration of the solute in the fluid, D the molecular diffusion coefficient, assumed constant in the fluid, S the solute concentration on the surface (i.e. concentration of the adsorbed solute), \mathbf{n} the unit normal to the boundary, α and λ the adsorption and desorption rates, respectively. The first equation in (1) describes solute transport governed by the advection-diffusion equation, while the second defines the boundary condition regulating the exchange between the fluid and the fluid/solid interface. The rate of change of surface concentration is defined by the difference between the rate at which solute concentration adheres to the boundary (αC) and the rate at which surface concentration desorbs into the fluid (λC). To satisfy mass balance principles, this rate of change must be equal to the diffusive flux of solute concentration occurring at the boundary ($-D\frac{\partial C}{\partial n}$). Problem (1) is completed by an appropriate set of initial and inlet/outlet boundary conditions. The system described is characterized by the following dimensionless numbers

$$Pe = \frac{\bar{L}\bar{u}}{D} \quad Da_a = \frac{\alpha \bar{L}}{D} \quad Da_d = \frac{\lambda \bar{L}^2}{D}$$
 (2)

where \bar{u} is the characteristic velocity and \bar{L} the representative length of the system. Pe represents the Péclet number, which describes the ratio between advection and diffusion processes.

 Da_a and Da_d are the adsorptive and desorptive Damköhler numbers, respectively. Da_a measures the ratio between adsorption reaction rate and diffusion rate, while Da_d compares the time scales associated with desorptive processes to diffusive ones.

2.1.1 Particle Tracking

The transport equation is solved through a numerical Lagrangian particle-based random walk method [32]. In this approach, the solute plume is discretized into a finite number of particles, each one representing a specific amount of solute mass. During each step Δt , the position of the particle \mathbf{x}_n and the time t_n are quantified as

$$\mathbf{x}_{n+1} = \mathbf{x}_n + \mathbf{u}\left(\mathbf{x}_n\right) \Delta t + \xi_n \sqrt{2D\Delta t}$$
(3)

$$t_{n+1} = t_n + \Delta t \tag{4}$$

where ξ_n is a random vector whose components are independent and identically distributed Gaussian variables with zero mean and unit variance and Δt is a time step. We assume here the velocity field \mathbf{u} is obtained by solving the steady state Navier-Stokes equations with an appropriate set of boundary conditions.

2.1.2 Adsorption/Desorption Modeling

Transport processes in the presence of sorption necessitate distinct boundary conditions due to the introduction of a substance flux from the fluid to the surface of the pores. The Robin boundary condition serves as a governing principle for regulating the concentration of the adsorbed chemical substance at a specific point on the pore surface. A particle crossing the solid boundary can be adsorbed with a probability P or reflected with a probability 1 - P. To the leading order, this probability can be computed as [10]

$$P = \alpha \sqrt{\frac{\pi \Delta t}{D}} \tag{5}$$

The second order approximation writes as

$$P^* = \frac{P}{1 + P/2} \tag{6}$$

The validity of these approximations hinges on the condition that P remains significantly smaller than one. In this work, adsorption probability is modeled by eq. (6). The value of P^* is compared to a random number U, drawn from a standard uniform distribution. If $U \geq P^*$ no sorption occurs and if $U < P^*$ the particle undergoes adsorption. In the event of adsorption, the particle spends a waiting time ζ on the liquid/solid boundary. Subsequently, it is released into the fluid following the standard reflection rule. This entire process can be conceptualized as a single step with a longer time duration:

$$t_{n+1} = t_n + \Delta t + \zeta_n \tag{7}$$

2.1.3 Time Increment

The choice of the time increment Δt in the implementation of the particle-tracking method is essential for accurately simulating the displacement of particles. We opt to impose Δt in a manner that constrains the maximum displacement d_{max} along each spatial direction. Given that the particle displacement \mathbf{d} encompasses both deterministic, equal to $\mathbf{u}(\mathbf{x}_n) \Delta t$, and

random, corresponding to $\xi\sqrt{2D\Delta t}$, components, we constrain d_{max} relying on a probabilistic approach, i.e.,

$$\Pr[\max(d_x, d_y, d_z) > d_{\max}] < p_{\alpha} \tag{8}$$

where p_{α} is the confidence level and $\mathbf{d}=(d_x,d_y,d_z)$. Here we assume that d_{max} is assigned in relation to the resolution employed to discretize the pore-scale geometry and velocity. For the deterministic term, the maximum displacement is contingent upon the velocity and is quantified as $max(\|\mathbf{u}\|)\Delta t$. The random component is associated with diffusion, and it is not feasible to establish a deterministic relationship between d_{max} and Δt . Given that the displacement along each spatial direction adheres to a normal distribution $N(0,\sigma^2)$, with $\sigma=\sqrt{2D\Delta t}$, a reasonable estimate for the maximum displacement due to diffusion is $2\sqrt{2D\Delta t}$, corresponding to a probability of 2.28% that the particle displacement exceeds 2σ . Consequently, we impose

$$max(\|\mathbf{u}\|)\Delta t + 2\sqrt{2D\Delta t} < d_{max} \tag{9}$$

and the following constraint is thus applied

$$\Delta t_T = \left(\frac{-\sqrt{8D} + \sqrt{8D + 4max(\|\mathbf{u}\|)d_{max}}}{2max\|\mathbf{u}\|}\right)^2$$
(10)

where Δt_T provides a limiting value for the discretization of advective diffusive transport. In addition, as discussed in Section 2.1.2, the time increment is further constrained by the approximation of adsorptive/desorptive processes through \mathbf{n} . Selecting an appropriate time increment is essential to ensure that P, defined in eq. (5), remains substantially smaller than 1. The time increment derived from the first order approximation of sorption probability in eq. (5) reads

$$\Delta t_R = \left(\frac{\bar{P}}{\alpha}\right)^2 \frac{D}{\pi} \tag{11}$$

where $\bar{P} \ll 1$ is a selected reference value for P, and Δt_R provides a reference value for the simulation of adsorption. The application of a constant time step throughout the simulation requires selecting the minimum value between (10)-(11), which can lead to a very large computational burden. Therefore, we define in the following an alternative discretization strategy employing a dynamic selection of the time step Δt_n .

Considering transport in the fluid phase, determining the time increment according to eq. (10) imposes a stringent constraint, corresponding to a worst-case scenario in terms of advective displacement $max(\|\mathbf{u}\|)$. However, particles may explore diffusion-dominated regions (e.g., cavities) which often are characterized by a considerable spatial dimension. Consequently, the length of the steps within diffusion-dominated regions greatly influences the algorithm's performance. A potential solution entails the dynamic computation of the time increment. In this framework, the idea behind eq. (10) is employed to compute a local Δt_n at each time step utilizing the velocity of the specific point where the particle is located, as opposed to the maximum velocity across the entire domain:

$$\Delta t = \left(\frac{-\sqrt{8D} + \sqrt{8D + 4\|u\| d_{max}}}{2\|u\|}\right)^{2}.$$
 (12)

Following this criterion, the time increment varies between advection and diffusion dominated regions, maintaining a statistically similar length of the displacement. In this work, we compare the results by computing the time increment following two strategies:

- 1. Static: a constant time increment is imposed as the minimum value between those given by eqs. (10)- (11). Such value of Δt is applied to each particle regardless of its position;
- 2. Dynamic: we partition in this case the pore space in two sub-domains, i.e. $\Omega_f = \Omega_{ff} \cup \Omega_{fs}$, where Ω_{fs} identifies a close-to-interface region and Ω_{ff} the rest of the fluid domain. The time step Δt_n is set equal to the one used in the static case close to the interface, i.e. $\Delta t_n = \Delta t_{fs}$ when the particle is located in the Ω_{fs} region, in order to simulate the particle's behavior near the discontinuity interface more accurately. Otherwise, when the particle is located in Ω_{ff} the time increment is computed in a dynamic way according to eq. (12). In the example discussed below (see Section 3) we employ a voxel-based discretization of the porous medium geometry. Therefore, we assign voxels having at least one face or edge lying on the liquid-solid interface to the close-to-interface region Ω_{fs} . The splitting approach employed here is commonly adopted when considering particle transport in the presence of interface phenomena, see e.g. [4].

2.2 Upscaled Spatial Markov Model

We present a trajectory-based Spatial Markov Model (tSMM) framework to upscale advection/diffusion transport and adsorption/desorption processes in porous media. We consider here transport over a periodic domain, i.e. considering a collection of periodic unit cells associated with spatial dimension L, where both geometry and velocity are periodic along the three spatial directions. The approaches described in 2.1.1-2.1.2 allow simulation of pore-scale processes, yet their application over vast spatial domains is computationally not affordable. The tSMM is grounded on the time-domain random walk method, whereby solute is discretized into particles, each representing a distinct mass quantity. We assume a one-dimensional setup where the average velocity field is aligned with the x-direction, thus the upscaled SMM model can be expressed as

$$x_i^{k+1} = x_i^k + L (13)$$

$$t_i^{k+1} = t_i^{k} + \tau_i^{k+1} \tag{14}$$

where i refers to the particle index, x_i^k and x_i^{k+1} represent the particle location at step k and k+1, respectively, t_i^k and t_i^{k+1} are the time associated with the particle at the step k and k+1, L is the spatial increment assumed equal to the length of the periodic cell.

The method is based on the direct simulation of a set of trajectories $S = \{s_1, \ldots, s_{N_{TT}}\}$, where N_{TT} represents the number of trajectories included in the set. For each trajectory in S we record four pieces of information resulting from the direct particle tracking simulation of transport across a single cell: the inlet $\mathbf{a}(s_i)$ and outlet $\mathbf{b}(s_i)$ locations, the travel time related to transport $\tau_T(s_i)$ and the number of sorption events $N_A(s_i)$. We then define a transition matrix T_{ij} indicating the probability of a particle to jump from one trajectory to another. Given two trajectories s_i and s_j , the probability T_{ij} of a particle to jump from i to j is assigned a value of 0 if the inlet point $\mathbf{a}(s_j)$ of the trajectory s_j does not rank among the N_{tr} closest starting positions to the final position $\mathbf{b}(s_i)$ of the trajectory s_i according to the Euclidean distance $Dist(\mathbf{b}(s_i), \mathbf{a}(s_j))$ between $\mathbf{b}(s_i)$ and $\mathbf{a}(s_j)$. We test two possible strategies to populate T_{ij} : a) uniform probabilities assigned to N_{tr} ranking as the closest to \mathbf{b}_i , b) weighting based on the inverse of the distance $Dist(\mathbf{b}(s_i), \mathbf{a}(s_j))$.

In summary, the implemented tSMM algorithm comprises the following steps:

- 1. An initial position \mathbf{x}^1 reflecting a prescribed inlet condition (e.g., as described in Section 3.3) is attributed to each particle;
- 2. For each particle, an initial trajectory is designated, chosen from the set of all possible trajectories. The selection process is based on finding the trajectory whose inlet location \mathbf{a}_i is closest to the initial position of the particle \mathbf{x}^1 . Consequently, the initial trajectory s_{j^1} is selected according to:

$$j^{1} = \underset{i}{\operatorname{argmin}} \left[Dist\left(\mathbf{x}^{1}, \mathbf{a}_{i}\right) \right]$$
 (15)

- 3. For k > 1 a trajectory s_{j^k} is selected based on the transition matrix **T**. The probability of choosing the trajectory j^k for a given particle at step k is determined by the element T_{j^{k-1},j^k} of the transition matrix.
- 4. The location x_i^k , the travel time t_i^k and total number of adsorption events $N_{A,i}^k$ of particle i are iteratively updated according to the property of trajectory s_{jk} , as follows

$$x_i^{k+1} = x_i^k + L (16)$$

$$N_{A,i}^{k+1} = N_{A,i}^{k} + N_{A}(s_{i}^{k}) \tag{17}$$

$$t_i^{k+1} = t_i^{k} + \tau(s_{ik}) \tag{18}$$

$$\tau(s_{j^k}) = \tau_T(s_{j^k}) + Z_i^k \tag{19}$$

$$Z_i^k = \sum_{n=1}^{N_A(s_{jk})} \zeta_n \tag{20}$$

where ζ_n are sampled from the density distribution $\psi(\zeta) = \lambda e^{-\lambda \zeta}$ [34]. Recording N_A allows repeating the same simulation for different values of the desorption rate λ , without the need of repeat the parameterization step.

Note that medium periodicity is assumed, since the transition probability T_{j^{k-1},j^k} is assigned based on inlet/outlet locations.

2.3 Quantities of Interest

We focus on the assessment of different quantities that define the advective/diffusive transport as well as the dynamics of adsorption/desorption processes. The performance of the tSMM to predict such phenomena is evaluated by comparing the tSMM results with the DNS outcomes. The appraised quantities are listed and described in the following.

2.3.1 Arrival Time Distribution

We evaluate the time t_f required for each particle to traverse a specified number of periodic units N_u along the x-direction. With reference to the dimensionless coordinates as defined in eq. (22), the distribution of the t_f is given by the conditional density $p_{t_f} = p(t|\tilde{X} = N_u)$, the latter being derived from the arrival time simulated by the model for each particle. The distribution is built by employing a binning algorithm histcounts provided by MATLAB, which optimizes the choice of the bin length in order to reveal the shape of the underlying probability density.

2.3.2 Adsorption Events and Time Delay

The number of adsorption events N_A constitutes a crucial outcome of our implemented model. Accurate estimation of N_A is essential, as each adsorption event induces a time delay in the particle's arrival time, as indicated in eq. (7). In our evaluation, we consider the overall number of adsorption events

$$N_{A,tot} = \sum_{i=1}^{N_p} \sum_{k=1}^{N_u} N_{A,i}^k$$
 (21)

where $N_{A,i}{}^k$ is the number of adsorption during the step k for the particle i and N_u is the considered number of steps. We consider the total delay Z for each individual particle by aggregating the delays experienced across each step k as expressed in eq. (20). The delay distribution p_Z can be estimated from the simulated particles' sample, relying on the same binning algorithm employed for the arrival times density.

3 Test Case

We consider advective/diffusive transport and adsorption/desorption processes of a solute in a three-dimensional porous medium. We posit Ω as a collection of identical periodic units, perpetually replicated throughout the spatial domain. Each periodic cell is a cube of size $L_x \times L_y \times L_z$. The cell is discretized by N_x, N_y, N_z cubic voxels of side Δ equal to 2×10^{-6} m in x, y, z direction, respectively. Computationally, void voxels are ascribed a value of 1, whereas solid voxels are assigned a value of 0.

Given the periodicity of the domain, we define dimensionless coordinates, which measure distances in terms of periodic units [9]

$$\tilde{x} = \frac{x}{L_x}, \quad \tilde{y} = \frac{y}{L_y}, \quad \tilde{z} = \frac{z}{L_z}$$
 (22)

3.1 Pore-Scale Setting

The computational porous domain is obtained by relying upon the pore structure generator algorithm presented in [31], the latter being a modified version of the algorithm in [21]. The algorithm here proposed enables generating a sample mimicking the topological and geometrical properties and the spatial statistics of a porous medium with physical properties indicated in Table 1. We define a set Ω_{Δ} , considering the discretization of the domain Ω in identical cubic cells (voxels) of size Δ . The algorithm comprises three main steps: (a) generate upon the set Ω_{Δ} a realization $r(\mathbf{x})$ of an uncorrelated random field that follows a uniform distribution $\mathcal{U}(0,1)$; (b) compute a topography $\Theta(\mathbf{x})$ representing the convolution between $r(\mathbf{x})$ and a deterministic kernel; (c) construct the set Ω_{Δ} by defining an indicator

function through the application of a threshold to the topography $\Theta(\mathbf{x})$, such thresholding defines pore and solid voxels. Further postprocessing is performed to eliminate disconnected pores. Details on the functioning of the pore structure algorithm are provided in [9, 31].

Table 1: Geometrical Characteristics of the Unit Cell

		parameter	SI units
Φ	0.30	Porosity	
Δ	2×10^{-6}	Spatial discretization along x, y, z	\mathbf{m}
l_c	1.51×10^{-5}	Representative pore length scale	m

The characteristic pore length scale l_c is determined by computing the empirical variogram of the topography Θ , the latter being defined as

$$2\gamma(h) = \frac{1}{|N(h)|} \sum_{i,j \in N(h)} (\Theta(\mathbf{x}_i) - \Theta(\mathbf{x}_j))^2$$
(23)

where $N(h) = \{(i, j) \mid ||\mathbf{x}_i - \mathbf{x}_j|| = h\}$, and i, j denote the indices of two observations and h is a lag distance. The representative pore length scale is identified as the variogram range, also referred as correlation length, here termed l_c .

The fluid velocity $u(\mathbf{x})$ is obtained by numerically solving the Navier-Stokes equations with Openfoam [24]. The numerical scheme provides a velocity value only on the voxels cell faces, consequently, the velocity field inside the voxels is obtained by interpolating the inlet and outlet velocity at the point location within the cell. No slip is applied on the liquid-solid boundary. The flow is computed assigning a one-dimensional pressure gradient aligned with the x-direction thus obtaining a one-dimensional upscaled transport process.

3.2 Initial Conditions: Flux Weighted Pulse

In this work we assume an initial scenario where a solute pulse is assigned at the inlet surface Σ_{in} of the first periodic cell

$$\Sigma_{in} = \mathbf{x} \in \mathbb{P}|x = 0, 0 \le y \le L_y, 0 \le z \le L_z \tag{24}$$

The initial concentration on Σ_{in} is determined according to the flux-weighted condition

$$C(\mathbf{x},0) \propto u_x(\mathbf{x},0) \quad \forall \mathbf{x} \in \Sigma_{in}$$
 (25)

The choice of this specific initial condition is motivated by the fact that it is expected to reproduce experimental conditions. Moreover, flux-weighted velocity are asymptotically attained by a set of Lagrangian particles [14]. In our particle tracking framework, the flux-weighted initial condition is obtained through the following steps:

- 1. For each cell index (1, j, k), a weight proportional to the x-component of the velocity at the inlet of the cell $u_x^{in}(1, j, k)$ is assigned. If $u_x^{in}(1, j, k)$ is negative, the weight is set to 0;
- 2. For each particle an initial cell index is randomly selected based on the weight assigned to each cell index as defined in Step 1;
- 3. The initial particle's position \mathbf{x}^1 with the chosen cell index $(1, j^1, k^1)$ is determined as

$$\mathbf{x}^1 = (1\Delta x, j^1 \Delta x, k^1 \Delta x) - \Delta x \mathcal{U}^3(0, 1) \tag{26}$$

where $\mathcal{U}^3(0,1)$ is a three-dimensional vector of uniformly distributed random numbers. This approach ensures that a distinct initial location is achieved, in the case two particles are assigned the same voxel.

3.3 Initial Conditions: SMM Training

Parameterization of the SMM also requires simulation of a set of particles across a single unit cell. To simulate the trajectories that are employed to parameterize the SMM model, we modify this inlet condition. In this case the flux intensity is balanced with the need to populate the inlet boundary locations: because diffusion is present, particles may visit diffusion-dominated regions. The particles are then distributed along the inlet face as:

- 20% uniformly distributed on the fluid portion of the inlet boundary of the domain;
- 80% distributed according to the flux-weighted initial condition discussed above (see Section 3.3).

4 Results

The presentation of the results is here split into two parts. First Section 4.1 is devoted to numerically assessing convergence of the pore-scale particle tracking modeling approach. Then, Sections 4.2-4.3 provide a discussion of the tSMM performance.

4.1 Pore-Scale Model Assessment

The particle's arrival time t_f (see Section 2.3.1) is employed as a fundamental metric to characterize transport, while the total number of absorptions $N_{A,tot}$ (see Section 2.3.2) is utilized for evaluating adsorptive processes. The analysis is performed on a three-dimensional domain as described in Section 3 and with the physical parameters reported in Table 2. We focus on advection-dominated transport in the presence of moderate sorption. The geometry of the porous domain and the corresponding velocity field are shown in Figure 1.

The simulation is conducted by assuming both a static and dynamic time increment as explained in Section 2.1.3.

Table 2: Size and Physical Properties of the Computational Domain for DNS Analysis

		Parameter	SI units
L_x	5.12×10^{-4}	Length of the domain region	m
Pe	100	Péclet number	
D	7.52×10^{-11}	Molecular diffusion coefficient	$\rm m^2/s$
α	2×10^{-7}	Adsorption rate	m/s
Da_a	0.0372	Adsorptive Damköhler number	
Δt_s	8.37×10^{-6}	Static increment time	\mathbf{s}
$ \bar{\mathbf{u}} $	5.3909×10^{-4}	Mean velocity	m/s

We assess first the impact of the number of particles N_p employed on the arrival time distribution. As depicted in Figure 2 (a), the distribution of particle arrival times exhibits disparities primarily at the tails when varying N_p between 10^3 and 5×10^5 . Notably, for

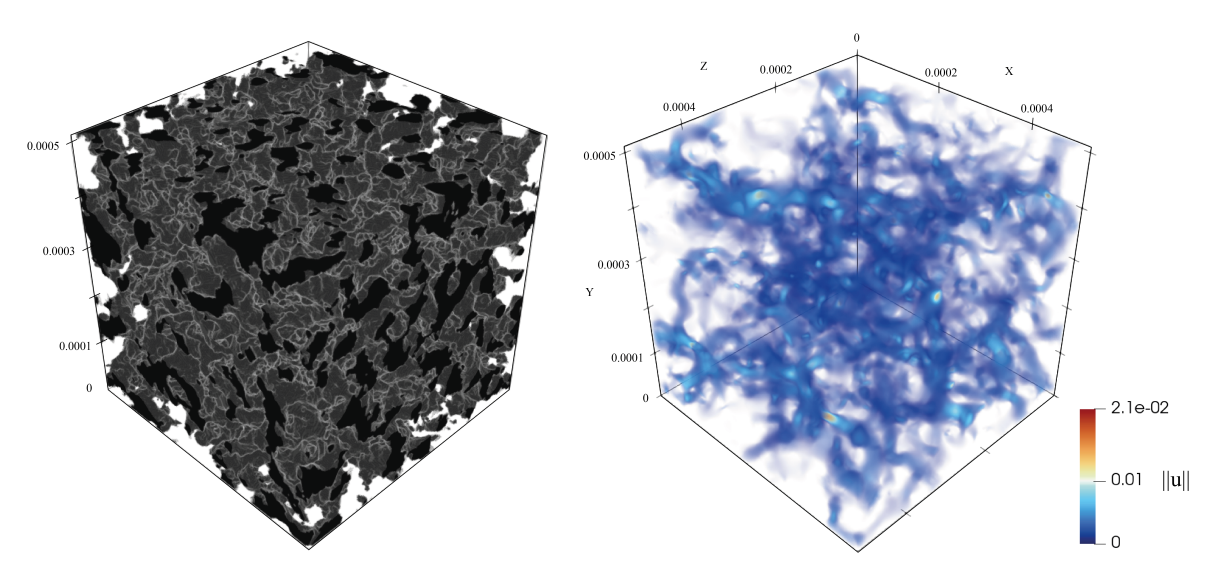


Figure 1: 3D visualization of the porous domain (left) and the velocity field (right) in [m/s]

smaller t_f values, the distributions closely overlap. The third quartile q_{75} of p_{t_f} is selected as a metric for comparing the model outcomes. From Figure 2 (b), we can observe that $q_{75}(p_{t_f})$ converges to approximately 1.13 for N_p greater than 1×10^5 , regardless of whether the static or dynamic time increment approach is employed. The two approaches offer comparable accuracy, but the dynamic approach presents the advantage of reducing computational time. Figure 3 compares the total computational time t_c required for the simulation in the two cases and allows appreciating that the computing time is approximately halved when using the dynamic time increment method compared to the static approach. In light of these findings, the subsequent analyses in Sections 4.2-4.3 are performed using the dynamic time increment approach.

The total number of adsorption events $N_{A,tot}$ is computed according to eq. (21). Results refer here to both the total number of sorption events and to the third quartile of the arrival time distribution $q_{75}(p_{t_f})$, taken as an indicator of the convergence of transport. Note that the time increment displayed in Figure 4 refers to the one applied in the region close to the solid-liquid interface. Both $N_{A,tot}$ and $q_{75}(p_{t_f})$ converge when the time increment Δt is smaller than 5×10^{-5} s. Generally, the total number of adsorption events displays greater dependence on Δt_{fs} . This is in line with the observation that the Δt value displayed in figure directly affects the simulation only close to the interface and therefore has a minor effect on arrival times (less than 5% variation is observed when Δt varies by more than two orders of magnitude).

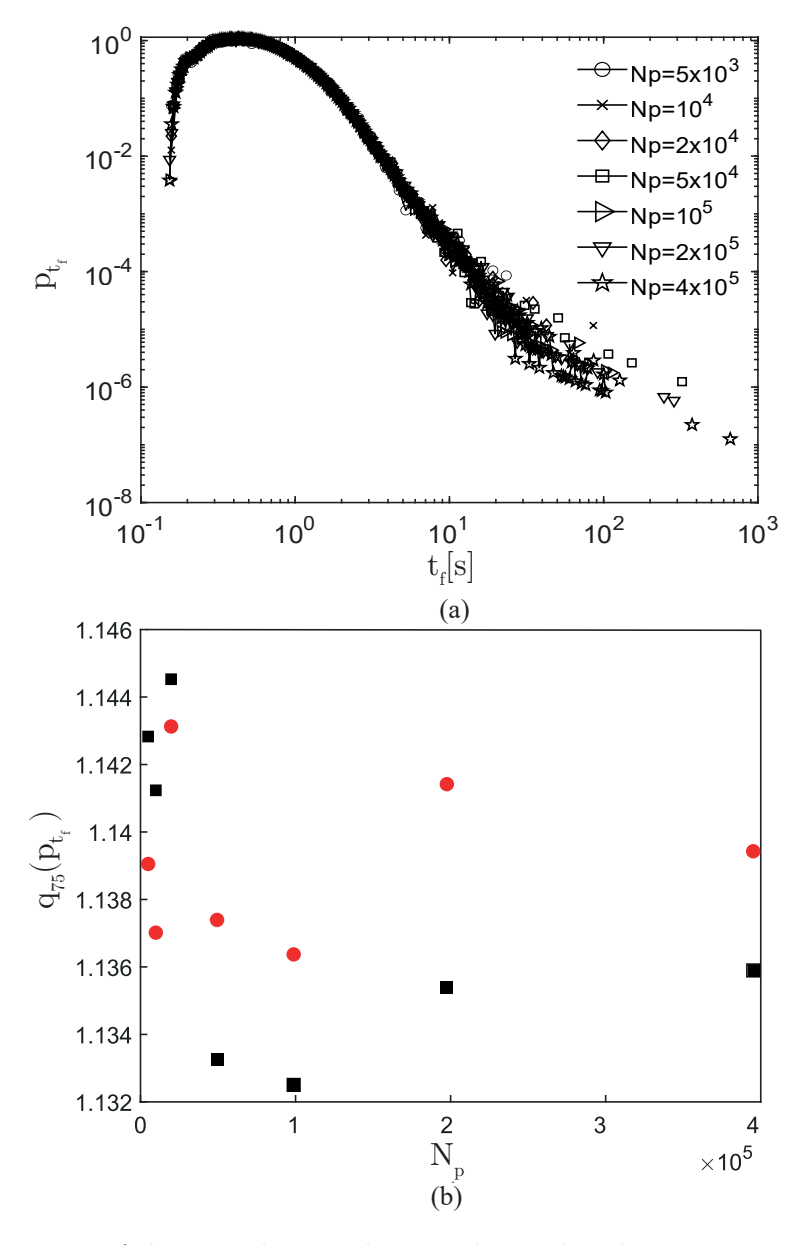


Figure 2: Comparison of the particle arrival times obtained with varying number of particles N_p : (a) arrival time distribution p_{t_f} , (b) third quantile q_{75} of p_{t_f} for the static (red dots) and dynamic (black squares) time increment approach

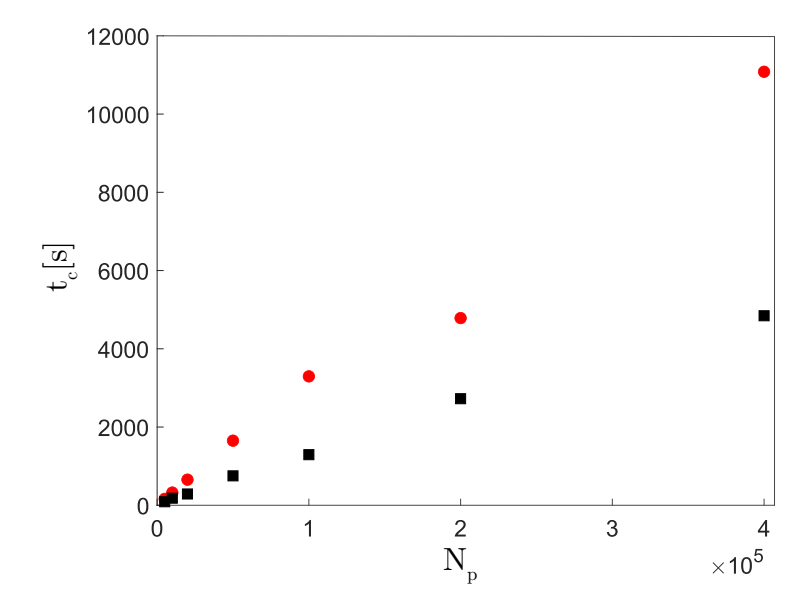


Figure 3: Computational time required to simulate particle transport across a single unit cells upon employing static (red dots) and dynamic (black squares) time step. Results are shown as a function of the number of particles N_p

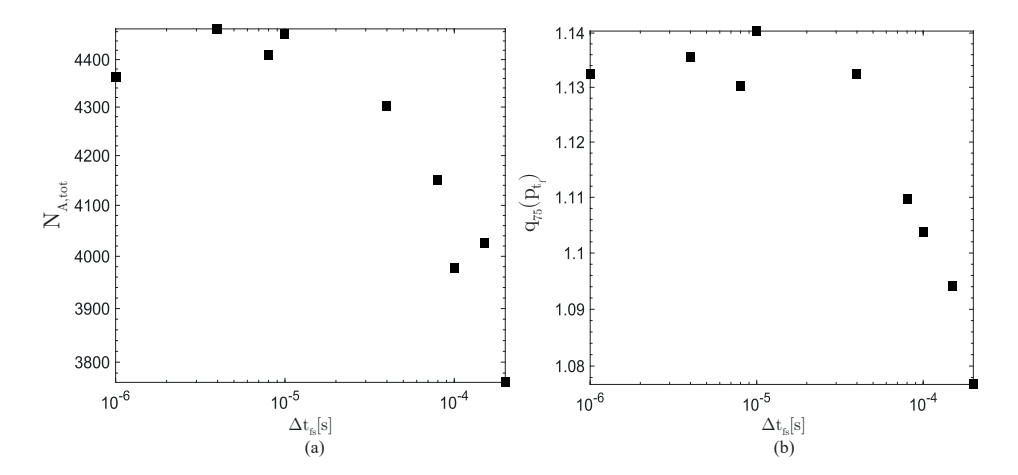


Figure 4: Total number of adsorption events $N_{A,tot}$ (a) and the third quantile $q_{75}(p_{t_f})$ of the distribution of p_{t_f} (b) as a function of the time step Δt_{fs} imposed in the close-to-interface fluid domain Ω_{fs} . Results are obtained employing a dynamic time stepping in the far-from-interface fluid domain Ω_{ff} .

4.2 SMM Upscaled Model

We analyze here results obtained through an upscaled SMM when simulating longitudinal transport across a collection of periodic unit cells, and we consider the impact of the parameter N_{tr} , i.e. the number of trajectories selected to assign the particle step, which ultimately leads to the definition of our transition matrix $\mathbf{T}_{i,j}$. We compare two scenarios: (a) the weighted case where $w_j \propto Dist(\mathbf{b_i}, \mathbf{a_j})^{-1}$, and (b) unweighted case where the same weight is attributed to each of the possible N_{tr} (see Section 2.2). The analysis is performed for three Péclet numbers, $Pe_1 = 50$, $Pe_2 = 100$, $Pe_3 = 200$, and varying N_{tr} between 10 and 500. The physical and computational parameters are reported in Table 3.

				Parameter	SI system
L_x		2.56×10^{-2}		Length of the domain	m
N_u		50		Number of unit cells	
	Pe_1	Pe_2	Pe_3		
Δt	3.69×10^{-5}	3.95×10^{-5}	4.156×10^{-5}	Time increment	S
D	1.50×10^{-10}	7.52×10^{-11}	3.76×10^{-11}	Diffusion coefficient	m^2/s
α	4×10^{-7}	2×10^{-7}	1×10^{-7}	Adsorption rate	m/s
Da_{α}		3.72×10^{-2}		Damökhler number	

Table 3: Physical and Computational Parameters for Assessing the Impact of the Number of Selected Trajectories

The accuracy of the SMM is assessed by comparing the probability distribution of t_f values estimated by the SMM with those obtained through DNS. The Hellinger distance (HD) is employed [20]

$$HD[q^*, q] = \frac{1}{\sqrt{2}} \sqrt{\sum_{i=1}^{N_b} (\sqrt{q_{i^*}} - \sqrt{q_{i}})^2}$$
 (27)

where q and q^* are the discrete probability distribution of the arrival time obtained by the SMM and the DNS, respectively, both discretized using N_b bins. HD is bounded between 0 and 1, where 0 indicates that the two distributions are indiscernible and 1 that they are maximally distant. From Figure 5 we observe that the HD values for the weighted scenario are consistently lower than those obtained in the unweighted case for all the analyzed numbers of selected trajectories. Specifically, for all the considered Péclet numbers, HD spans from 0.025 to 0.06 for the unweighted case and from 0.02 to 0.05 for the weighted case. These values are indicative of satisfactory accuracy. Note that considering two samples of size 10^5 drawn from an identical Gaussian distribution yields $HD \approx 0.015$ (the value is indicated by a continuous red line Figure 5). This reference value quantifies the effect of finite sample size on the employed metric. Note that considering two samples of size 10^5 drawn from an identical Gaussian distribution yields $HD \approx 0.015$ (the value is indicated by a continuous red line Figure 5). This reference value quantifies the effect of finite sample size on the employed metric.

For each number of selected trajectories, HD tends to increase in the x-direction, with best-performing simulations displaying a stable HD value after 30 unit cells. On average, for a higher number of selected trajectories, the increase in HD in the x-direction is more pronounced for higher Péclet numbers. For lower N_{tr} values and under the same weighted approach, the tSMM provides similar accuracy in predicting the particle arrival time distribution for different Péclet numbers. The results obtained are compared in Figure 5 with the HD value (red thick line) between samples drawn from identical normal distributions for a sample size of 10^5 .

In Figure 6, the Hellinger distance is presented for both the weighted and unweighted approaches, considering various N_{tr} values and two different positions within the computational domain: (a) at x = 5L and (b) at x = 50L. Lower HD values are consistently observed in the weighted scenario compared to those found in the unweighted case for a given domain location and across all considered Péclet numbers. This observation supports the findings in Figure 5 and suggests that weighting the trajectories based on the distance between the subsequent trajectory inlet and outlet locations provides similar accuracy regardless of the number of selected trajectories, especially close to the inlet (i.e. at distance 5L). Each HD-trajectory

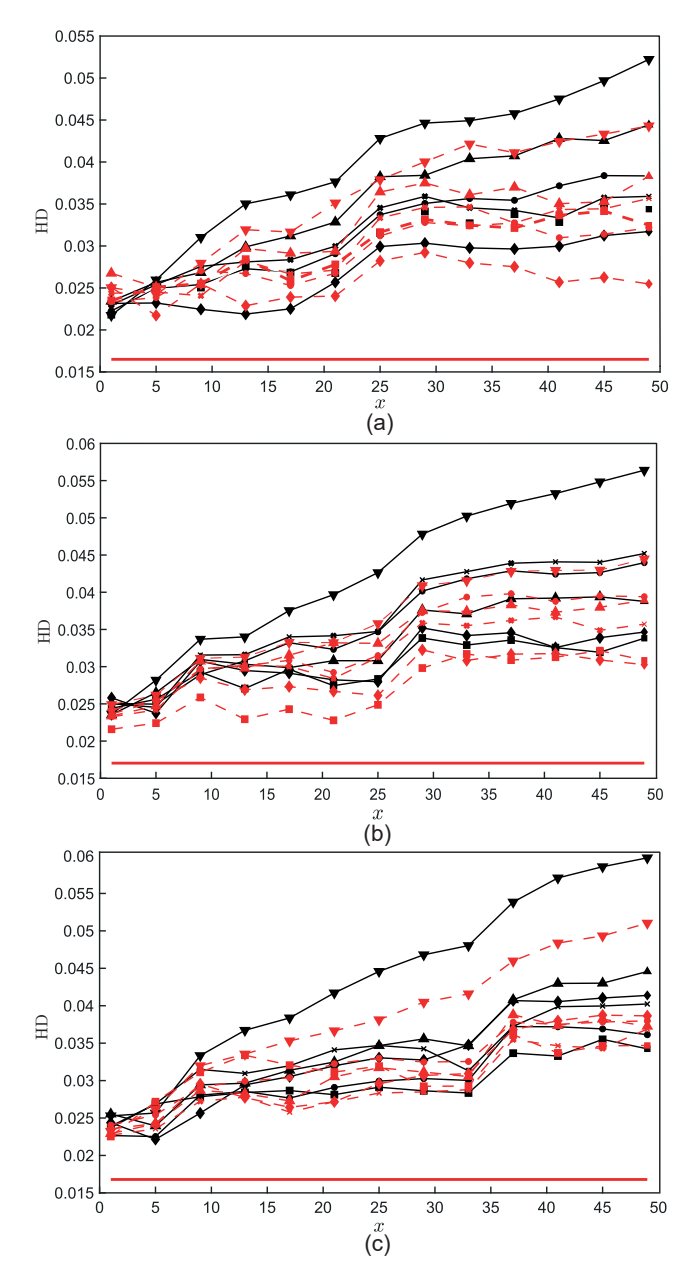


Figure 5: Comparison of the HD values between the probability distribution of the particles' arrival times obtained by the SMM (q) and the DNS (q^*) in the weighted case (red dashed line) and unweighted case (black solid line) along the x-direction for a different number of selected trajectories for (a) Pe = 50, (b) Pe = 100, (c) Pe = 200: (\circ) 10, (\Box) 30, (\diamondsuit) 50, (\triangle) 80, (\times) 100, (\bigtriangledown) 500 trajectories. The red solid line corresponds to the HD value between two normal probability distributions for a sample size of 10^5 elements.

number curve exhibits an increase in HD with the number of trajectories (N_{tr}) , with minor fluctuations as the Péclet number increases due to reduced diffusive effects. The minimum point of each curve represents the number of selected trajectories that offers the highest accuracy in estimating the distribution of particle arrival times. For location x = 50L, the minimum is observed at $N_{tr} = 50$ for both Péclet numbers equal to 50 and 100. For Pe = 200, the highest accuracy is found for a number of trajectories equal to 30. However, there is no clear correlation between the optimal number of trajectories and the Péclet number based on these results. In the tested conditions, results reveal that the weighted and unweighted cases display similar accuracy when considering the best case results. Yet, the weighted case is capable of maintaining a similar performance for a wider interval in terms of N_{tr} . Hence, for the weighted case the accuracy exhibits low sensitivity to this particular parameter. In conclusion, the weighted method appears to be a more precautionary approach, ensuring good accuracy regardless of the number of selected trajectories. Therefore, the results presented in the following are obtained relying upon the weighted method.

Next, we investigated the impact of the number of particles employed in the simulation N_p on the accuracy of the particles' arrival time predictions from the tSMM. Based on the lower Hellinger distance values observed in Figure 7, the tSMM simulations are conducted under the weighted scenario. Here, HD is computed for the probability distribution of particle arrival times, as defined in eq. (27), by fixing $N_{tr} = 10$ and $N_{TT} = 10^5$, while progressively incrementing N_p in the SMM. A reference DNS simulation run with 10^5 particles is used for estimating HD. As shown in Figure 7, the Hellinger distance values are consistently low and decrease with increasing N_p , indicating good agreement between the SMM and DNS. The convergence appears to stagnate when HD approaches 0.02, i.e. close to the minimum reference value obtained above.

The impact of the number of selected trajectories on the estimation of the total number of adsorption events $N_{A,tot}$, computed according to eq. (21), is further evaluated. For each Péclet number, the $N_{A,tot}$ values obtained in the SMM are compared with those derived from the DNS. The percentage error $E_{\%}$, quantified as in eq. (28), is employed as metric to assess the accuracy of the results.

$$E_{\%} = \frac{N_{A,tot}^* - N_{A,tot}(N_t)}{N_{A,tot}^*} 100$$
 (28)

where $N_{A,tot}^*$ and $N_{A,tot(N_t)}$ are the number of adsorption events obtained in the DNS and tSMM (using N_{tr} selected trajectories), respectively. As displayed in Figure 8, the percentage error for Pe=50 ranges from 0.3% to 2% when N_{tr} is assumed equal to 50 and 100, respectively. Higher $|E_{\%}|$ values are observed for a Péclet number of 100 and 200, with $|E_{\%}|$ varying between 0.9 and 2.7 for Pe=100 and between 0.1% and 6.2% for Pe=200. These results indicate that the mean percentage error increases as the Péclet number increases. The optimal value of N_{tr} is consistent with the findings related to the particle arrival times for Pe=50, while for Pe equal to 100 and 200 N_{opt} different results are obtained for the two outputs. This suggests that the optimal number of trajectories may vary depending on the specific transport and adsorption characteristics of the system, particularly as the Péclet number increases. We observe, however, that all results display relatively small deviations, thus supporting the general robustness of the tSMM approach in reproducing the DNS results with acceptable accuracy.

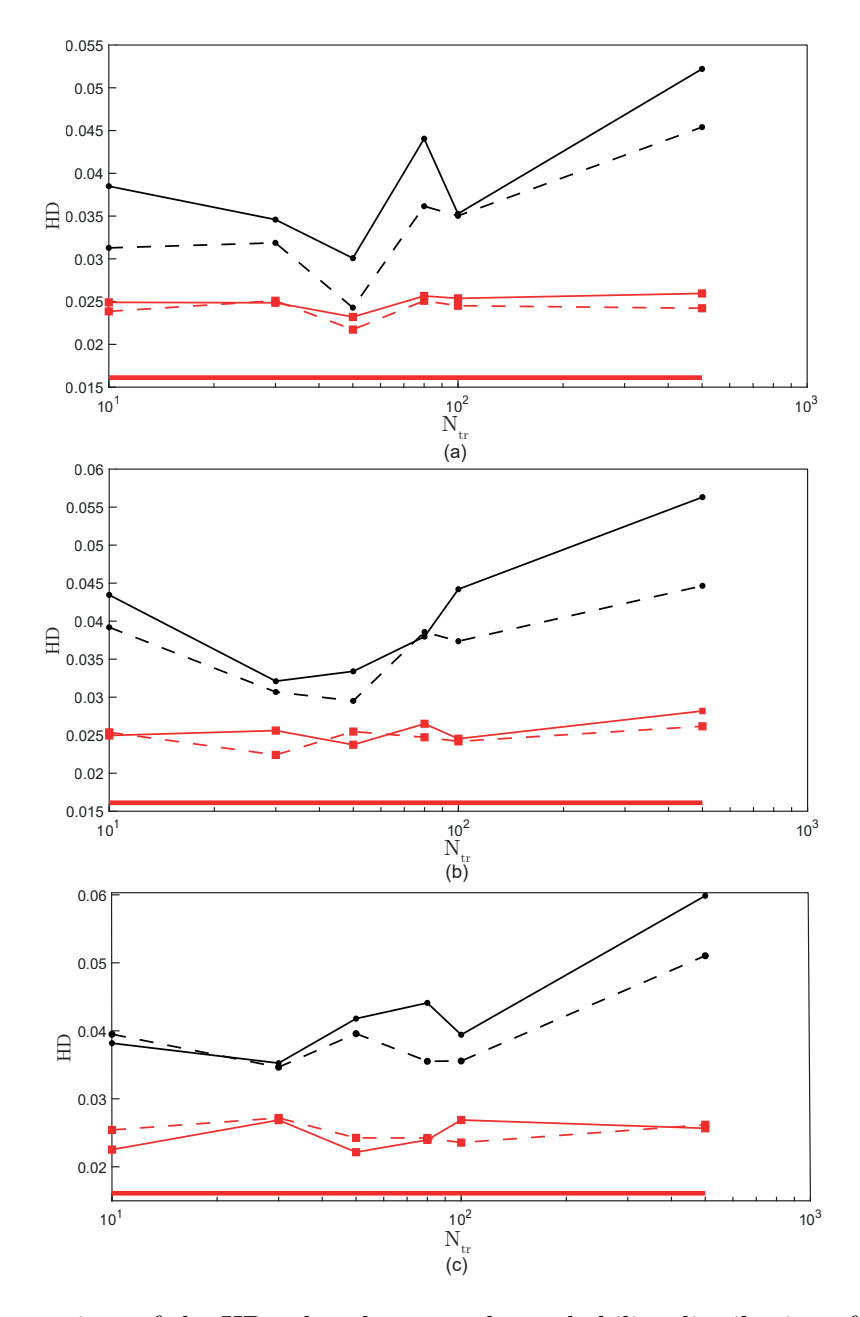


Figure 6: Comparison of the HD values between the probability distribution of the particles arrival times obtained by the SMM (q) and the DNS (q^*) in the weighted case (dashed line) and unweighted case (solid line) for a varying number of selected trajectories at location x = 5L (red lines) and x = 50L (black lines). Different Péclet numbers are assessed: (a) Pe = 50; (b) Pe = 100; (c) Pe = 200. The red solid line corresponds to the HD value between two samples of size 10^5 drawn from the same normal probability distribution. Results refer to single realizations.

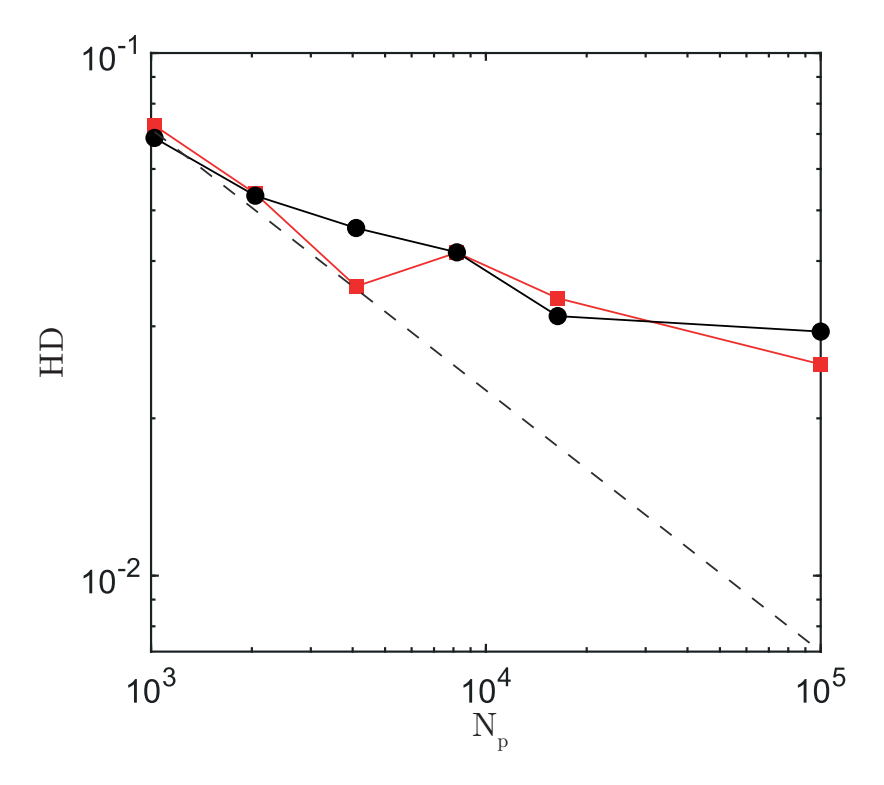


Figure 7: Comparison of the HD values between the probability distribution of the particles' arrival times (p_{t_f}) obtained by the SMM (q) and the DNS (q^*) in the weighted case at location x = 5L (red line) and x = 10L (black line). The dashed line represents the trend $HD \propto N_p^{-0.5}$

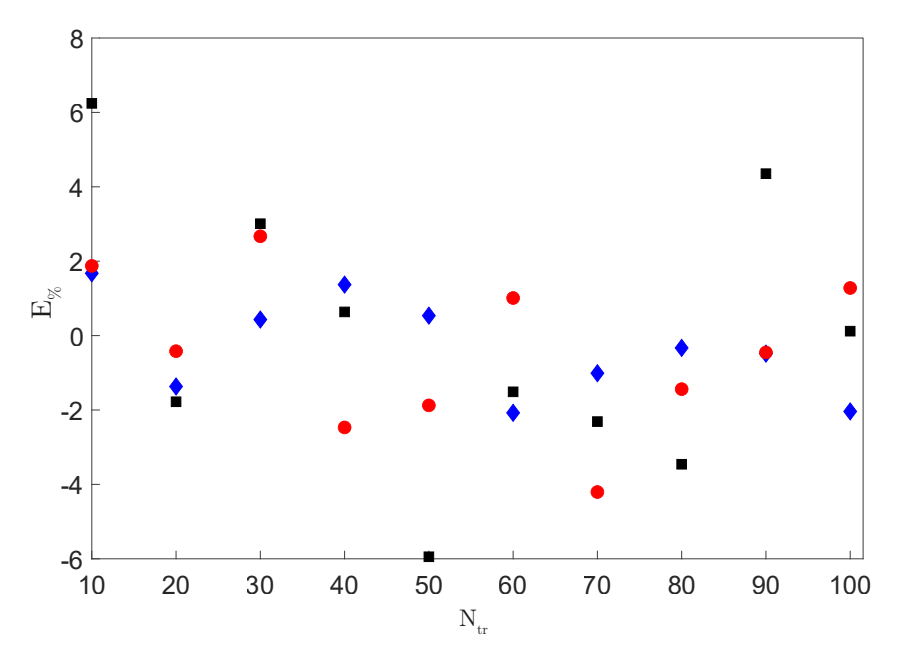


Figure 8: Comparison of the percentage error $E_{\%}$ between the total number of the adsorption events computed by the SMM $N_{A,tot}$ and the DNS $N_{A,tot}^*$. Results are shown as a function of N_{tr} and Pe equal to 50 (blue diamonds), 100 (red dots) and 200 (black squares)

4.3 Adsorption/Desorption Analysis

We discuss here the application of tSMM in predictive mode. The analysis is conducted using the same computational domain introduced earlier (Table 2) and composed of 50 periodic unit cells. The tSMM simulations are conducted by using the weighted approach with a number of selected trajectories equal to 50, based on results in Section 4.2. We compare tSMM with DNS results in terms of particle arrival time t_f (see Section 2.3.1), delay ζ due to the particle adsorption (see Section 2.3.2) and total arrival time t_{tot} , the latter being calculated as

$$t_{tot} = t_f + Z \tag{29}$$

First, the delay resulting from adsorptive events is computed according to eq. (20) with an assumed value of $Da_d = 0.013$. The distribution of t_f , ζ and t_{tot} for the domain location x = 1L, x = 30L and x = 50L are presented in Figure 9. The tSMM approximates the DNS results well, particularly with respect to the delay and total time distribution. Minor differences emerge in the particle arrival time distribution at x = 30L and x = 50L for the tail of the delay and total arrival time. For these time intervals, the tSMM slightly overestimates the arrival time in comparison to the predictions made by DNS. This observed behavior is primarily attributable to sampling errors, particularly for those trajectories affected by long travel times due to diffusion processes in low velocity regions. This result does not significantly impact the overall alignment between the DNS and SMM outcomes. This analysis provides evidence of the SMM's capability to accurately predict both transport and adsorptive/desorptive phenomena.

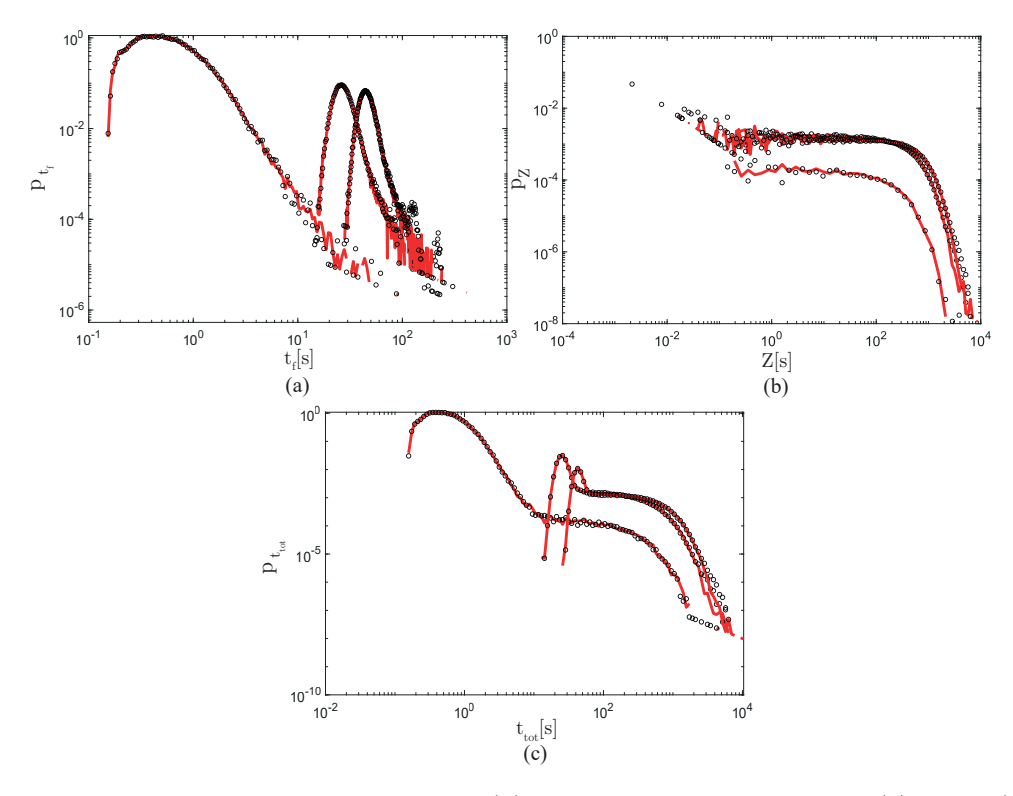


Figure 9: Comparison of the distribution of (a) the particles' arrival time, (b) delay (c) total particles' arrival time between the DSN (red solid line) and the SMM (black dots) at distances 1L, 30L and 50L

Our investigation extends to the evaluation of the arrival time distribution $(p_{t_{\text{tot}}})$ at distinct locations within the computational domain, specifically at x = 1L, 10L, and x = 50L encompassing various combinations of adsorptive and desorptive Damköhler numbers and

Péclet numbers of 100. The analysis presented in Figure 10 clearly illustrates that an increase in the adsorptive Damköhler number results in prolonged particle arrival times at a given position. Particles are more likely to be absorbed as Da_a increases, leading to a delay in their arrival at the outlet of the periodic unit. When $Da_a = 1.1$, a distinctive pattern emerges in $p_{t_{\text{tot}}}$ at x = 1L. A prominent peak is observed at lower arrival times followed by a near constant trend up to $t_{\text{tot}} \approx 10^3$. At the same location with $Da_a = 0.005$ the arrival time distribution is characterized by a single peak occurring at lower t_{tot} . Similar concentration patterns are evident at locations x = 30L and x = 50L. At these locations, unique peaks are observed in $p_{t_{\text{tot}}}$, particularly noticeable when $Da_a = 1.1$, for both the adsorptive Damköhler numbers considered. For a given Da_a , increasing Da_d results in a reduction of the arrival time, with a more significant effect observed for $Da_a = 1.1$.

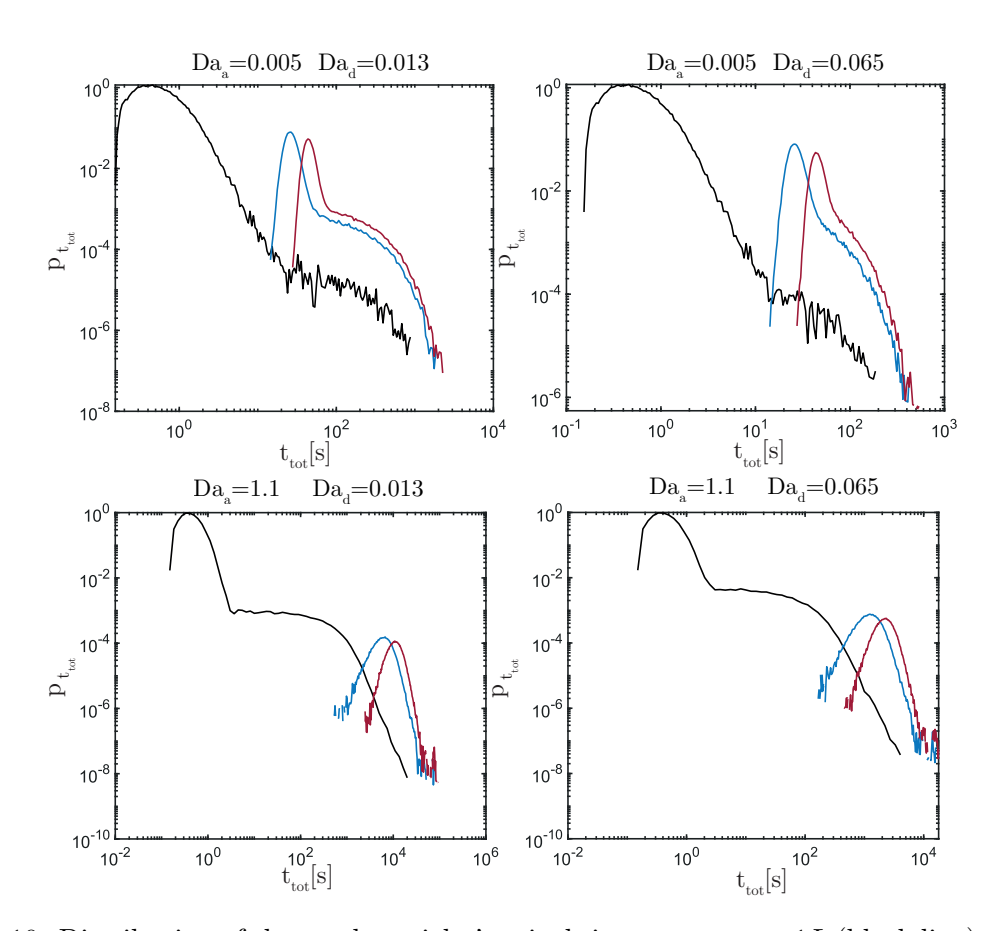


Figure 10: Distribution of the total particles' arrival time $p_{t_{\text{tot}}}$ at x = 1L (black line), x = 30L (blue line) and x = 50L (red line) for different combinations of the adsorptive Damköhler number Da_a and desorptive Damköhler number Da_d

5 Discussion and Conclusions

The work proposes a numerical tool based on the Spatial Markov model (SMM) to predict transport and adsorption/desorption processes in a three-dimensional porous media. The framework is constructed using the trajectory-based spatial Markov model (tSMM) proposed in [38] where high-resolution trajectories generated through an advective-diffusive random walk across a singular periodic flow element are stitched together subsequently to upscale transport and surface reactive processes to significantly larger scales. The algorithm is an

extension of that presented in [9], the latter being limited only to a two-dimensional domain. Optimization strategies, including the dynamic selection of the time increment, result in a computational time that is tenfold lower than the original code.

The dynamic time increment speeds up the computation in the presence of large areas dominated by diffusion. The results from the tSMM are benchmarked against the outcomes derived from the direct numerical simulation performed on the same porous domain. Additional optimization strategies can be applied to improve the performance of the implemented algorithm.

Trajectory selection is rigorously evaluated to upscale the simulation effectively to larger scales. We assess the impact of the weighting approach in the selection of the trajectories to be assigned to each particle on the modeling results, especially in terms of particle arrival time. The 'weighted scenario', where weights are determined proportionally to the distance between the final position and the inlet point of the trajectory, proves more accurate than the 'unweighted case' where a uniform weight of 1 is assigned to each trajectory. The 'optimal number' of trajectories varied with Péclet numbers. Overall the weighted approach displayed low sensitivity to the number of trajectories employed to simulate transitions across different transport steps, thus showing robustness with respect to this particular numerical parameter.

The tSMM's predictive performance for adsorption and desorption phenomena is evaluated and compared against DNS results. Strong alignment between SMM and DNS outcomes was observed in terms of particle arrival times, delay due to adsorption, and total arrival times, indicating the SMM's capability to accurately predict both transport and adsorptive/desorptive phenomena. Arrival time distributions are analyzed at different locations within the computational domain for various combinations of adsorptive and desorptive Damköhler numbers. Higher adsorptive Damköhler numbers led to prolonged particle arrival times. The desorptive Damköhler number's impact is more pronounced at higher adsorptive Damköhler numbers, emphasizing the interplay between adsorption and desorption processes.

In conclusion, our approach provides a low-cost approximation of solute transport coupled with sorption processes that can be employed to test sorption/desorption in column settings for a variety of reaction rates and transport setups at lower computational cost, as compared to a pore-scale simulation. In this sense, our model could be employed to facilitate experimental design or optimization where multiple realizations and parametric analyses may be necessary. The presented approach assumes linear sorption and desorption processes, and thus cannot be directly used to model the effects of competitive sorption and sorption site availability. Yet, recent studies have discussed methods to incorporate nonlinear reaction rates into Lagrangian solvers [3], thus opening a pathway towards extending tSMM to model these phenomena.

Acknowledgements

G.M. Porta acknowledges funding from the European Union's Horizon 2020 research and innovation programme under the Marie Skłodowska-Curie grant agreement No 872607. We acknowledge Matteo Radice and Gael R. Guedon for their contribution in setting up the numerical methodology.

Data Availability

All data and codes used to process or generate the data are available in a publicly accessible repository: Porta, Giovanni Michele; Baioni, Elisa (2025), "SMM", Mendeley Data, V1, doi: 10.17632/djg35czznj.1 or https://data.mendeley.com/preview/djg35czznj?a=4f70ec08-3446-4efa-b809-438d6fd65713

Author Contributions

GMP: Corresponding author. Contribution to conceptualization of the research idea, supervision of the project, interpretation of the results, and preparation of the manuscript. EB: Computational analyses and preparation of the manuscript.

References

- [1] A. Adrover, C. Venditti, and G. Desmet. An alternative general model for the effective longitudinal diffusion in chromatographic beds filled with ordered porous particles. Journal of Chromatography A, 1715, 2024. doi: 10.1016/j.chroma.2023.464598.
- [2] T. Aquino. Equilibrium distributions under advection—diffusion in laminar channel flow with partially absorbing boundaries. *Journal of Fluid Mechanics*, 985:A16, 2024. doi: 10.1017/jfm.2024.294.
- [3] T. Aquino. Coupled nonlinear surface reactions in random walk particle tracking. Advances in Water Resources, 185:104656, 2024.
- [4] E. Baioni, A. Lejay, G. Pichot, and G. M. Porta. Modeling diffusion in one dimensional discontinuous media under generalized permeable interface conditions: Theory and algorithms. SIAM Journal on Scientific Computing, 46(4):A2202–A2223, 2024. doi: 10.1137/23M1590846.
- [5] I. Battiato and D. Tartakovsky. Applicability regimes for macroscopic models of reactive transport in porous media. *Journal of Contaminant Hydrology*, 120-121:18–26, 2011. ISSN 0169-7722. doi: https://doi.org/10.1016/j.jconhyd.2010.05.005. Reactive Transport in the Subsurface: Mixing, Spreading and Reaction in Heterogeneous Media.
- [6] D. A. Benson, R. Schumer, M. M. Meerschaert, and S. W. Wheatcraft. Fractional dispersion, lévy motion, and the made tracer tests. *Transport in porous media*, 42:211–240, 2001.
- [7] B. Berkowitz, H. Scher, and S. Silliman. Anomalous transport in laboratory-scale, heterogeneous porous media. *Water Resources Research*, 36:149 158, 2000. doi: 10.1029/1999WR900295.
- [8] B. Berkowitz, A. Cortis, M. Dentz, and H. Scher. Modeling non-fickian transport in geological formations as a continuous time random walk. *Reviews of Geophysics*, 44(2), 2006.
- [9] E. Bianchi Janetti, T. Sherman, G. R. Guédon, D. Bolster, and G. M. Porta. Upscaling of solute plumes in periodic porous media through a trajectory-based spatial markov model. *Water Resources Research*, 56(12):e2020WR028408, 2020.
- [10] G. Boccardo, I. M. Sokolov, and A. Paster. An improved scheme for a robin boundary condition in discrete-time random walk algorithms. *Journal of Computational Physics*, 374:1152–1165, 2018.
- [11] D. Bolster, Y. Méheust, T. Le Borgne, J. Bouquain, and P. Davy. Modeling preasymptotic transport in flows with significant inertial and trapping effects—the importance of velocity correlations and a spatial markov model. *Advances in water resources*, 70:89–103, 2014.

- [12] O. Cirpka, M. Stettler, and M. Dentz. Spatial markov model for the prediction of traveltime-based solute dispersion in three-dimensional heterogeneous media. Water Resources Research, 58, 2022. doi: 10.1029/2022WR032215.
- [13] F. Delay, A. Kaczmaryk, and P. Ackerer. Inversion of a lagrangian time domain random walk (tdrw) approach to one-dimensional transport by derivation of the analytical sensitivities to parameters. Advances in Water Resources, 31:484–502, 2008. doi: 10.1016/J.ADVWATRES.2007.10.005.
- [14] M. Dentz, P. K. Kang, A. Comolli, T. Le Borgne, and D. R. Lester. Continuous time random walks for the evolution of lagrangian velocities. *Physical Review Fluids*, 1(7): 074004, 2016.
- [15] M. Dentz, A. Comolli, V. Hakoun, and J. J. Hidalgo. Transport upscaling in highly heterogeneous aquifers and the prediction of tracer dispersion at the made site. *Geophysical Research Letters*, 47(22):e2020GL088292, 2020.
- [16] J. Dreuzy, A. Rapaport, T. Babey, and J. Harmand. Influence of porosity structures on mixing-induced reactivity at chemical equilibrium in mobile/immobile multi-rate mass transfer (mrmt) and multiple interacting continua (minc) models. Water Resources Research, 49:8511 – 8530, 2013. doi: 10.1002/2013WR013808.
- [17] N. B. Engdahl and T. Aquino. Upscaled models for time-varying solute transport: Transient spatial-markov dynamics. *Advances in Water Resources*, 166:104271, 2022. ISSN 0309-1708. doi: https://doi.org/10.1016/j.advwatres.2022.104271.
- [18] A. Golbabai and K. Sayevand. Analytical modelling of fractional advection-dispersion equation defined in a bounded space domain. *Math. Comput. Model.*, 53:1708–1718, 2011. doi: 10.1016/j.mcm.2010.12.046.
- [19] R. Haggerty and S. M. Gorelick. Multiple-rate mass transfer for modeling diffusion and surface reactions in media with pore-scale heterogeneity. Water Resources Research, 31 (10):2383–2400, 1995.
- [20] E. Hellinger. Neue begrundung der theorie quadratischer formen von unendlichvielen veränderlichen. *Journal Für Die Reine Und Angewandte Mathematik*, pages 210–271, 1909. doi: 10.1515/crll.1909.136.210.
- [21] J. D. Hyman and C. L. Winter. Stochastic generation of explicit pore structures by thresholding gaussian random fields. *Journal of Computational Physics*, 277:16–31, 2014.
- [22] T. Le Borgne, J.-R. de Dreuzy, P. Davy, and O. Bour. Characterization of the velocity field organization in heterogeneous media by conditional correlation. *Water resources research*, 43(2), 2007.
- [23] T. Le Borgne, M. Dentz, and J. Carrera. Lagrangian statistical model for transport in highly heterogeneous velocity fields. *Physical review letters*, 101(9):090601, 2008.
- [24] O. Ltd. Openfoam programmer's guide (version 9.0). OpenCFD Ltd, 2023.
- [25] A. Massoudieh, M. Dentz, and J. Alikhani. A spatial m arkov model for the evolution of the joint distribution of groundwater age, arrival time, and velocity in heterogeneous media. *Water Resources Research*, 53(7):5495–5515, 2017.

- [26] M. Meerschaert and C. Tadjeran. Finite difference approximations for fractional advection-dispersion flow equations. *Journal of Computational and Applied Mathematics*, 172:65–77, 2004. doi: 10.1016/J.CAM.2004.01.033.
- [27] S. Most, D. Bolster, B. Bijeljic, and W. Nowak. Trajectories as training images to simulate advective-diffusive, non-fickian transport. *Water Resources Research*, 55(4):3465–3480, 2019.
- [28] S. Painter, V. Cvetkovic, and O. Pensado. Time-domain random-walk algorithms for simulating radionuclide transport in fractured porous rock. *Nuclear Technology*, 163:129 – 136, 2008. doi: 10.13182/NT08-A3976.
- [29] D. Pedretti, D. Fernàndez-Garcia, X. Sanchez-Vila, D. Bolster, and D. Benson. Apparent directional mass-transfer capacity coefficients in three-dimensional anisotropic heterogeneous aquifers under radial convergent transport. Water Resources Research, 50:1205 – 1224, 2014. doi: 10.1002/2013WR014578.
- [30] A. Puyguiraud, P. Gouze, and M. Dentz. Pore-scale mixing and the evolution of hydro-dynamic dispersion in porous media. *Physical Review Letters*, 126(16):164501, 2021.
- [31] M. Radice. Particle-based simulation and upscaling of transport processes in porous media. 2021. URL https://hdl.handle.net/10589/177465.
- [32] H. Risken and H. Risken. Fokker-planck equation. Springer, 1996.
- [33] T. Sherman, A. Fakhari, S. Miller, K. Singha, and D. Bolster. Parameterizing the spatial markov model from breakthrough curve data alone. Water Resources Research, 53(12): 10888–10898, 2017.
- [34] T. Sherman, A. Paster, G. Porta, and D. Bolster. A spatial markov model for upscaling transport of adsorbing-desorbing solutes. *Journal of contaminant hydrology*, 222:31–40, 2019.
- [35] T. Sherman, N. Engdahl, G. Porta, and D. Bolster. A review of spatial markov models for predicting pre-asymptotic and anomalous transport in porous and fractured media. *Journal of contaminant hydrology*, page 103734, 2020. doi: 10.1016/j.jconhyd.2020.103734.
- [36] N. Sund, D. Bolster, and C. Dawson. Upscaling transport of a reacting solute through a peridocially converging-diverging channel at pre-asymptotic times. *Journal of contaminant hydrology*, 182:1–15, 2015. doi: 10.1016/j.jconhyd.2015.08.003.
- [37] N. Sund, G. Porta, D. Bolster, and R. Parashar. A lagrangian transport eulerian reaction spatial (laters) markov model for prediction of effective bimolecular reactive transport. Water Resources Research, 53(11):9040–9058, 2017.
- [38] N. L. Sund, G. M. Porta, and D. Bolster. Upscaling of dilution and mixing using a trajectory based spatial markov random walk model in a periodic flow domain. *Advances in water resources*, 103:76–85, 2017.
- [39] J. Tecklenburg, I. Neuweiler, J. Carrera, and M. Dentz. Multi-rate mass transfer modeling of two-phase flow in highly heterogeneous fractured and porous media. *Advances in Water Resources*, 91:63–77, 2016. doi: 10.1016/j.advwatres.2016.02.010.
- [40] E. E. Wright, N. L. Sund, D. H. Richter, G. M. Porta, and D. Bolster. Upscaling mixing in highly heterogeneous porous media via a spatial markov model. *Water*, 11(1):53, 2018.

- [41] J. Zhan, W. Jiang, and Z. Wu. Reactive transport in open-channel flows with bed adsorption and desorption. *Journal of Hydrology*, 632:130855, 2024. ISSN 0022-1694. doi: https://doi.org/10.1016/j.jhydrol.2024.130855.
- [42] L. Zhang, M. A. Hesse, and M. Wang. Transient solute transport with sorption in poiseuille flow. *Journal of Fluid Mechanics*, 828:733–752, 2017. doi: 10.1017/jfm.2017. 546.
- [43] Y. Zhang, M. Meerschaert, and R. Neupauer. Backward fractional advection dispersion model for contaminant source prediction. Water Resources Research, 52:2462 – 2473, 2016. doi: 10.1002/2015WR018515.
- [44] A. Zoia, C. Latrille, and A. Cartalade. Nonlinear random-walk approach to concentration-dependent contaminant transport in porous media. *Physical review. E, Statistical, nonlinear, and soft matter physics*, 79 4 Pt 1:041125, 2008. doi: 10.1103/PhysRevE.79.041125.
- [45] A. Zoia, M. Néel, and A. Cortis. Continuous-time random-walk model of transport in variably saturated heterogeneous porous media. *Physical review. E, Statistical, nonlinear, and soft matter physics*, 81 3 Pt 1:031104, 2009. doi: 10.1103/PhysRevE.81.031104.